



The impact of residual stress on resonating piezoelectric devices

Glenn Ross^{a,*}, Hongqun Dong^a, Cyril Baby Karuthedath^b, Abhilash Thanniyil Sebastian^b, Tuomas Pensala^b, Mervi Paulasto-Kröckel^a

^a Department of Electrical Engineering and Automation, Aalto University, P.O. Box 13500, FIN-00076 Aalto, Finland

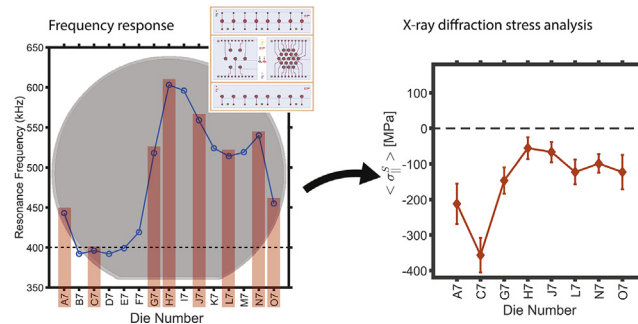
^b VTT Technical Research Centre of Finland, Espoo, Finland

HIGHLIGHTS

- Piezoelectric micromachined ultrasonic transducers (PMUTs) were fabricated using an AlN piezoelectric layer
- PMUTs have varying frequency along the length of the wafer, ranging from 400 to 600 kHz
- X-Ray Diffraction (XRD) was used to analyze the residual stresses present in several PMUTs located along the processed wafer
- Results showed there was a residual stress variation along the wafer, which correlated with the varying resonance frequency. Biaxial compressive residual stress values measured by XRD was in the range from -357 MPa to -56 MPa
- Resonating piezoelectric devices require well defined operating frequencies, therefore this work demonstrates the importance of studying not only global stresses (from methods such as wafer curvature), but also local residual stresses

GRAPHICAL ABSTRACT

Piezoelectric micromachined ultrasonic transducers (PMUT)



ARTICLE INFO

Article history:

Received 2 August 2020

Received in revised form 27 August 2020

Accepted 3 September 2020

Available online 09 September 2020

ABSTRACT

Resonating piezoelectric devices, such as aluminum nitride (AlN) piezoelectric micromachined ultrasonic transducers (PMUTs), display superior performance to previous generations of resonating microelectromechanical systems (MEMS). However, the quality of the piezoelectric thin film can greatly impact operating characteristics, such as the resonant frequency. Several AlN PMUT devices fabricated on the same silicon wafer exhibited a range of resonance frequencies (400–600 kHz), indicating that there is nonuniformity across the processed wafer. AlN film nonuniformity is likely introduced during the reactive sputtering process. Two key parameters identified as influencing the resonance frequency include: (i) the membrane diameter and (ii) residual stress. This work focuses on the residual stress, and uses X-ray diffraction technique (XRD) to determine the in-plane biaxial residual stress values, as a function of die position on the wafer. Results show that there is a compressive stress gradient along the wafer, ranging from -357 MPa to -56 MPa. A plot of in-plane biaxial residual stress as a function of resonance frequency shows a relation between the measured stress and frequency. As resonating piezoelectric devices require well defined operating frequencies and bandwidths, this work demonstrates the importance of studying not only global stresses, but also local residual stresses.

* Corresponding author.

E-mail address: glenn.ross@aalto.fi (G. Ross).

1. Introduction

Piezoelectric devices are natural candidates for microelectromechanical systems (MEMS) due to their intrinsic coupling of both electrical and mechanical properties. This allows for a piezoelectric material to either (i) mechanically deform when subjected to an electric field or (ii) generate an electric field when deformed. This opens a broad range of applications that can exploit the piezoelectric effect, such as sensors, actuators, oscillators and filters. Historically devices using the piezoelectric effect were fabricated from offcuts of bulk material. However, for MEMS the development of stable reproducible thin films using common complementary metal-oxide semiconductor (CMOS) compatible processes has allowed a broad range of possibilities in many different application fields. One obvious field of development is in efficiency improvements of inertial sensors that are based on capacitive actuation. More exotic examples where piezoelectric materials are being developed is in the field of environmental energy harvesting for autonomous MEMS. These could eventually lead to self-sufficient clusters of off-the-grid MEMS sensors for environmental monitoring, just one example [1–3].

Resonating piezoelectric devices account for a large fraction of piezo-MEMS currently under development, and are an example how piezoelectric materials excel in performance. One application of these is the piezoelectric micro-machined ultrasonic transducer (PMUT), which outperforms the capacitive version that can suffer from low sensitivity, high bias voltage requirements and greater fabrication complexity [4,5]. A typical PMUT structure consists of a layer of piezoelectric material sandwiched between two electrodes and mounted on a membrane that allows the suspended film to deflect. An example of a PMUT structure can be seen in Fig. 1. The piezoelectric

layer acts as both an ultrasonic actuator and sensor. As a generator the piezoelectric film is exposed to an electric field causing it to deform so that the suspended membrane can be excited at its resonance frequency, creating an ultrasonic wave. On the sensor side, ultrasonic stimulation of the membrane causes the film to deform generating an electric field in the piezoelectric material. There are several piezoelectric materials suitable for use in PMUT devices, such as aluminum nitride (AlN), lead zirconate titanate (PZT) and zinc oxide (ZnO). AlN has many attractive features making it the most desirable for a low-cost highly integrated MEMS resonator, these are: reproducible deposition, CMOS process compatibility, high hardness and stiffness, and low relative permittivity [2,6].

The deposition of high-quality thin-film AlN is achieved by several different methods, the two most popular are chemical vapor deposition (CVD) and physical vapor deposition (PVD). CVD methods, such as Metal-organic vapor phase epitaxy (MOVPE), can form exceptionally high crystal quality on appropriate seeding substrates. However, they can often suffer from significant stresses due to the high deposition temperatures required (>1000 °C). In contrast, PVD methods such as magnetron sputtering have been shown to deposit good quality AlN at lower temperatures (400–500 °C), and have the ability to adjust the film stresses by optimizing the sputtering parameters. Sputtering of AlN is done through a process of reactive sputtering, where sputtered aluminum is exposed to and reacts with nitrogen before condensing on the substrate. In this process the greatest impact on residual film stresses is how energetic the ion bombardment is, and the subsequent densification of the AlN film, which can cause a range of tensile to compressive residual stresses. These processes can be optimized by tuning the substrate potential. Film inhomogeneity

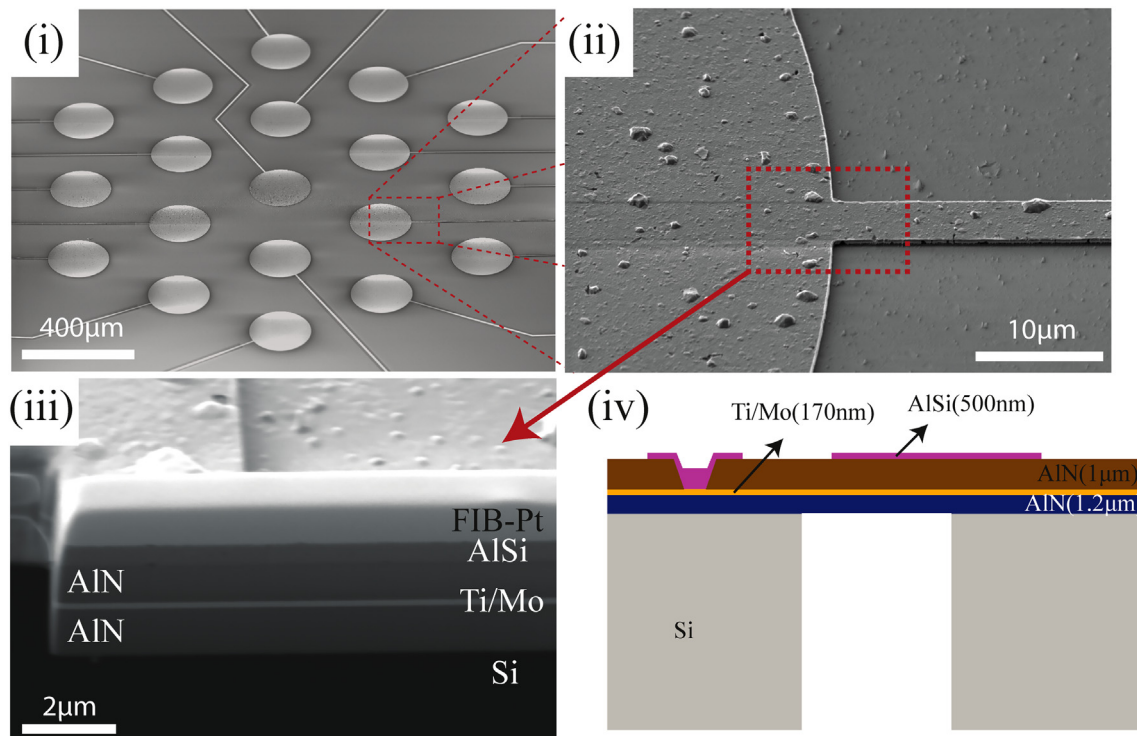


Fig. 1. (i) is a tilted SEM micrograph of the 19-element PMUT, (ii) is a magnified micrograph of the edge of an element, (iii) FIB cross-sectional micrograph highlighting the layer stack and (iv) illustrates the cross-section of a PMUT element.

can be produced if these parameters are not uniform across the substrate, and lead to potential stress gradients across the AlN film [2,7,8].

Classical plate theory for a circular plate that takes pre-tension into account can be seen in the equation of motion (Eq. 1). The plate pre-tension term is T_e , it is the sum of the pressure by plate thickness ($T_e = \sum_i \sigma_i h_i$), is the tension formed in the plate caused by residual stress, D_e is flexural rigidity and ρ_i is the area plate density ($\rho_i = \sum_i \rho_i h_i$) of the i -th layer of the membrane.

$$D_e \nabla^4 w - T_e \nabla^2 w + \rho_h \frac{\partial^2 w}{\partial t^2} = f(r, \theta, t) \quad (1)$$

Solving the above equation of motion enables one to find the resonance frequencies of circular plates. The resonance frequencies can be determined by Equation (2). Where $\omega_{n,m}$ is the natural frequency of a two-dimensional plate where n, m are the mode indices, $\lambda_{n,m}$ is a resonant mode constant and r is the radius of the plate. If the pre-tension term T_e is sufficiently small, the dominating impact is from the resonant mode constant and the flexural rigidity as seen in Eq. (2). However, when the residual stress magnitude increases the dominating factor will be the pre-tension term. This can, depending on the magnitude of residual stress, change the frequency response significantly [9,10].

$$\omega_{n,m} = \sqrt{\frac{\lambda_{n,m}^4 D_e}{\rho_i r^4} + \frac{\lambda_{n,m}^2 T_e}{\rho_i r^2}} \quad (2)$$

A common method for understanding the residual stress impact on circular resonating PMUTs is by solving the classical plate equations of motion and analytically modeling the behavior, such as the resonance frequency and plate deflection. Two such studies include the work of Dangi and Pratap [9] and Sammoura et al. [10]. The Dangi and Pratap study presented parametric plots of the resonance frequency and center point deflection as a function of radius and pre-tension of a PMUT acting as a transmitter, receiver, and a transceiver. Their results showed the coupled effects of the radius and the pre-tension, where a change in these parameters impacted the resonance frequency. The analytical results of the study were verified experimentally by fabricating two PZT based PMUT sample sets, one where the pre-tension was effectively zero (plate behavior) and one with significant tensile stress (membrane behavior). The magnitude of impact on the resonance frequency depended on whether the PMUT experienced plate or membrane behavior. In both cases an increasing pre-tension increased the resonance frequency. Sammoura et al. solved the equations of motion analytically for a circular plate using Green's function and modelled a PZT based PMUT. The theoretical model was applied to a PMUT immersed in water and a mechanical impedance plot was generated. The resonance impedance spectra were presented as a function of compressive, neutral, and tensile pre-tension; results showed that the resonance frequency decreased for compressive and increased for tensile stresses. Additionally, the study determined the zero-bias displacement of the plate due to residual stress and compared it with an experimentally measured sample using profilometry. The results were in good agreement with a plate deflection of 5.15 μm due to residual stress.

Optimization of the resonance frequency of a resonating piezoelectric device can be achieved through stress engineering the pre-tension term. As the pre-tension term is a function of the residual stress of each layer, a stress value for each layer can be selected to achieve a desired resonance frequency. One example of such an approach is when the PZT layer is under tensile stress and a thermal SiO_2 supporting layer is deposited with a compressive stress, effectively resulting in a net-zero pre-tension term [11]. This approach requires an understanding of how each layer contributes to the pre-tension term, and effectively excludes methods that give an average residual stress value

over the entire resonating PMUT, such as wafer curvature and plate deflection methods. Residual stresses can also have significant negative effects on piezoelectric devices. Such as with inhomogeneities in the deposited thin-films and the resulting residual stress profile, which can challenge the frequency matching of resonating devices. In more extreme cases, excessive compressive stress can result in buckling of a resonating membrane.

This work studies the AlN PMUT devices presented in [12], with a focus on the correlation between the samples position on a wafer and the residual stress. The work hypothesized that the frequency variation observed along the length of the wafer was due to a non-uniform stress profile parallel to the main silicon wafer flat. The resonance frequency variation observed ranged from less than 400 kHz to a maximum of over 600 kHz, with the designed resonance frequency of 400 kHz. X-ray diffraction (XRD) methods are used to study the impact of residual stress on the resonance frequency of the piezoelectric-AlN layer. This demonstrates the importance of taking residual stress into account when designing and fabricating piezoelectric resonating devices, such as PMUTs.

2. Materials and methods

PMUTs used in this work were based on sputter deposited c-axis orientated AlN. A comprehensive study of the design, simulation, fabrication, and characterization of the devices studied in this work can be found in [12]. Devices were fabricated on a 400 μm thick double-sided polished (DSP) silicon wafer. A 1.2 μm thick AlN passive layer was sputtered followed by the deposition of the bottom electrode (Ti seeded Mo), 20 nm and 150 nm for Ti and Mo respectively. Next, 1 μm c-axis orientated AlN piezoelectric material was deposited by sputtering onto the bottom electrode. Finally, a top electrode of 500 nm thick AlSi (1% Si) was deposited. Backside lithography and deep-reactive ion etching with a 294 μm target diameter cavity was carried out to release the membrane. A target resonance frequency of 400 kHz was designed based on Multiphysics modeling. A SEM micrograph of a 19-element PMUT, with a magnified cross-section of a single element can be seen in Fig. 1(i-iii). A dual-beam (SEM-FIB) JEOL JIB-4700F was used for cross-sectioning and imaging. A schematic of a single element including the material stack can be seen in Fig. 1(iv). Wafer curvature measurements were carried out using a thermal stress measurement tool from Toho Technologies (FLX 2320-S).

XRD measurements were performed using the Rigaku SmartLab with a 9 kW rotating Cu anode operating at 45 kV and 200 mA with Cu $K\alpha$ radiation at a wavelength of 1.54056 Å. XRD was performed in two principle modes (i) wide-area reciprocal space mapping (RSM) and (ii) in-plane symmetrical scans. The wide-RMS maps used a parallel beam with convergent focusing incidence optics and a two-dimensional wide-area (100 μm^2) semiconductor detector. Multiple scans were made at increasing sample tilting angles (S_3 to S_1). The scans were stitched together, and the units were converted from goniometer to reciprocal space units. The residual stress measurements were made in the in-plane symmetrical scan mode, which was carried out in a parallel beam condition. The incident optics included a 0.5° soller slit, a 0.05 mm incident slit and a 5 mm length limiting slit to confine the beam within the sample, this results in a sample surface spot size of 41 mm^2 . The receiving optics included a $K\beta$ -filter (Ni foil), a 0.5° parallel slit analyzer receiver, and a HiPix-3000 photon counting detector operating in 0D mode. To reduce instrumental effects on the peak position three approaches were taken, (i) a parallel beam condition was used, (ii) a silicon reference was measured, and (iii) all samples were measured with the same optics alignment conditions. A parallel beam avoids any shift in 2θ due to sample alignment issues. The silicon reference was used to correct shifts in 2θ due to parallel slit analyzer misalignment using the method described in [13].

XRD is a suitable method for determining the strain properties of the AlN piezoelectric thin film, as it can selectively probe in sufficiently high

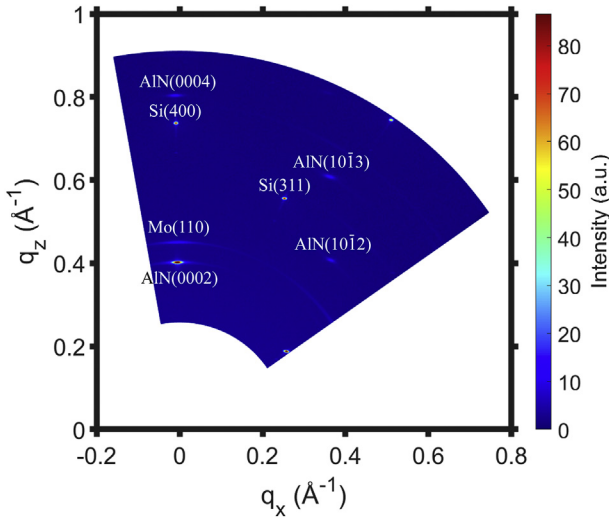


Fig. 2. Wide-area reciprocal space map (RSM) of sample O7.

resolution the relevant crystalline properties. A wide-area RSM of sample O7 can be seen in Fig. 2. The wide-area RSM shows several important crystallographic properties of the sample. Both the support and the piezoelectric AlN thin-film layers exhibit highly c-axis orientated texturing. Additionally, although not observable in the RSM, there is no AlN in-plane or fiber texturing, which is characteristic of AlN films grown by the reactive magnetron sputtering technique [2]. The other significant reflection observed in the RSM is in the molybdenum, which exhibited preferential (110) texturing when seeded by a thin Ti layer normal to the Si(100) substrate. The challenge with this particular structure is that two layers of AlN are present in the thin-film stack, an AlN passive layer and the active piezoelectric AlN layer. In the out-of-plane configuration both AlN layers contribute to the diffraction pattern observed in Fig. 2, however only the piezoelectric AlN layer is of interest for accurate X-ray diffraction stress determination (to avoid any peak shift from multilayer diffraction contribution).

In the in-plane configuration the incident angle is small resulting in a smaller penetration depth. A schematic of the in-plane configuration, with the relevant angles in the specimen reference frame (S_1 - S_3), is shown in Fig. 3 (i). With this configuration the incident angle is optimized in order to probe the piezoelectric layer without penetrating to the lower AlN layer. Using the Beer-Lambert law and linear absorption

coefficients (μ) of 136 cm^{-1} for Al(Si), 119 cm^{-1} for AlN, 1618 cm^{-1} for Mo, and 912.824 cm^{-1} for Ti [14,15], the intensity of the diffracted beam at the Ti/AlN (passive layer) interface would be: 88.0% and 0.2% of the incident beam for the out-of-plane ($\omega_{\text{AlN}(0002)} = 18.05^\circ$) and in-plane ($\omega = 0.35^\circ$) configurations respectively. Nonetheless, to confirm there is limited contribution from the AlN passive layer, in-plane measurements were made with a slowly increasing incident angle. The polycrystalline Mo(110) reflection was used as an indicator of the penetration depth. Fig. 3 (ii) shows diffractograms with increasing incidence angle. The AlN(1000) reflection on the left is located at $2\theta = 33.3^\circ$ and Mo(110) on the right is located at $2\theta = 40.5^\circ$. In the figure there is little effect on the AlN(1000) intensity at increasing incidence ω angle. On the other hand, as the angle is increased so does the intensity of the Mo(110). An angle of $\omega = 0.35^\circ$ was chosen as the fixed incidence angle for all the measurements, as it had shown to have minimal Mo(110) intensity. This would ensure that there is little to no contribution to the measured intensity from the AlN passive layer.

To determine the stress-strain values from the measured diffraction data, Bragg's law is utilized to relate the peak position to the interplanar spacing, as seen in Eq. (3). Refinement of the peak positions and measurement estimated standard deviations (ESD) was carried out using GSAS-II [16].

$$2d^{hkl} \sin \theta = n\lambda \quad (3)$$

where d^{hkl} [nm] is the interplanar spacing, θ [°] is the half angle between the incident beam and normal to the diffracting beam, n is the integer order of reflection and λ [nm] is the wavelength of the X-rays. The AlN film has the wurtzite-type structure (space-group, $P6_3mc$) [17] which belongs to the hexagonal crystal system. The relationship between the interplanar spacing d^{hkl} , the lattice constants a and c , and the indices of h, k, l can be found from Eq. (4) [18]. To determine the direction dependent (function of ψ) diffraction strain the measured interplanar spacings determined from Eq. (3) together with the strain-free interplanar spacing are used in Eq. (5).

$$\frac{1}{d^{hkl}{}^2} = \frac{4}{3} \left(\frac{h^2 + hk + k^2}{a^2} \right) + \frac{l^2}{c^2} \quad (4)$$

$$\varepsilon_\psi^{hkl} = \frac{d_\psi^{hkl} - d_0^{hkl}}{d_0^{hkl}} \quad (5)$$

where h, k, l are the Miller indices, a [nm] and c [nm] are the a- and c-lattice constants respectively. As there were no powder samples of

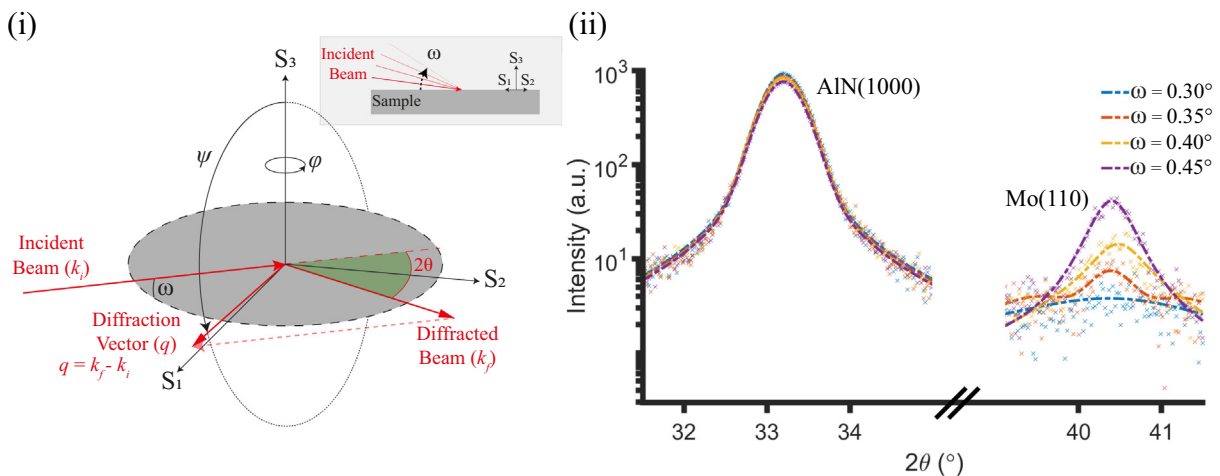


Fig. 3. (i) is a vector schematic of the in-plane configuration will all relevant angles, including a cross-sectional illustration of the increasing incident angle ω and (ii) are the results from determining the incident angle in order to illuminate only the active AlN layer. The first peak is the AlN(1000) reflection located at 2θ of 33.3° and the second peak Mo(110) located at 2θ of 40.5°

Table 1
X-ray Elastic Constants (XEC) calculated for *hk0* and *hk1*.

$S_1 (\times 10^{-6} \text{MPa}^{-1})$		$S_2/2 (\times 10^{-6} \text{MPa}^{-1})$	
<i>hk0</i>	<i>hk1</i>	<i>hk0</i>	<i>hk1</i>
-0.880	-0.885	4.345	4.326

AlN available, the strain-free lattice constants were selected from literature. The strain-free lattice constants for w-AlN used were 3.11197 (2) and 4.98089(4) Å for a_0 and c_0 respectively [19].

As the sputtered AlN exhibits fiber texturing and hexagonal symmetry around the *c*-axis, this results in elastic isotropy in the Basal plane. There is a reduction in the stress-strain parameter dependence on the measurement directions, therefore the non-zero stress component is $\langle \sigma_{11} \rangle = \langle \sigma_{22} \rangle = \langle \sigma_{\parallel} \rangle$ and there is no rotational dependence in the measurement direction $\varphi = 0$. To determine the lattice constants, and subsequently the rotationally symmetric biaxial residual stress, several in-plane (*hk0*) and near in-plane (*hk1*) specimen poles (nine in total), were measured due to the limitation in diffracted intensity. To determine the residual stress from the measured elastic strain, X-ray elastic constants (XEC) S_1^{hkl} and S_2^{hkl} using Eshelby-Kröner grain interaction model are used and can be seen in Eq. (6) [20–23]. Although AlN is elastically anisotropic a quasi-isotropic approach has been applied as there is neglectable elastic anisotropy within the measurement range from *hk0* to *hk1*. The XEC are defined as $S_1^{hkl} = -v^{hkl}/E^{hkl}$ and $\frac{1}{2}S_2^{hkl} = \frac{1+v^{hkl}}{E^{hkl}}$, where E^{hkl} and v^{hkl} are the crystallographic direction dependent Young's modulus and Poisson's ratio, which are determined from the single crystal stiffness tensor with the following constants required for hexagonal symmetry, $c_{11} = 345$, $c_{12} = 125$, $c_{13} = 120$, $c_{33} = 395$, and $c_{44} = 118$ GPa [24]. The values of the calculated XECs used in this work are in Table 1.

$$\epsilon_{\psi}^{hkl} = \left(2S_1^{hkl} + \frac{1}{2}S_2^{hkl} \sin^2 \psi \right) \langle \sigma_{\parallel}^S \rangle \quad (6)$$

A least-squares analysis was made to minimize (χ^2) the difference between the calculated strain from Eq. (6) and the measured strain in Eq. (5). From the analysis it is possible to fit the rotationally symmetric biaxial residual stress $\langle \sigma_{\parallel}^S \rangle$ parameter in the specimen reference frame.

Table 2
Incremental wafer curvature measurements of control wafers during PMUT process control.

Structure	Bow x [μm]	Bow y [μm]	σ_{S_x} [MPa]	σ_y [MPa]
Si/AlN	4.46	4.59	27	27
Si/AlN/Ti/Mo	6.05	9.11	-24	23
Si/AlN/Ti/Mo/AlN ^a	30.53	31.96	-1	-1
Si/AlN/Ti/Mo/AlN/Al ^a	13.57	18.76	-16	-15

^a Measured on PMUT designed patterned wafers.

To improve the quality of the analysis a normally distributed variability based on the measurement errors by the ESD was used for ω_i^2 . Error bars presented in the results reflect the standard errors for parameter estimates in the least-squares analysis. The least-squares relationship can be seen in Eq. (7).

$$\chi^2 = \sum_i \omega_i^2 \left[\epsilon_{\psi}^{calc} \left(\langle \sigma_{\parallel}^S \rangle, hkl, \psi \right) - \epsilon_{\psi}^{meas} (hkl, \psi) \right]^2 \quad (7)$$

3. Results and discussion

Results for the resonance frequency of the fabricated PMUT devices showed significant variation along the horizontal direction of the wafer. A layout of the measured devices and the results of the resonance frequency measurements can be seen in Fig. 4. The die numbers measured and analyzed in this work are highlighted in Fig. 4 (ii). The authors in [12] speculate that the resonance variation comes from the variation in the cavity diameter and/or residual stresses in the membrane. That study showed that the variation in the cavity diameter alone could not account for the wide variation, therefore the residual stress was the most likely candidate.

To measure the residual stress in a multi-layer sample is not a trivial task and most popular methods for determining stress, such as wafer curvature, only account for global stresses. This would neglect local and interfacial stresses and/or those within thin-film layers. During process control of PMUT fabrication, control wafers are used to design a desired residual stress in the thin-film stack. Table 2 shows the results of the residual stresses, determined from wafer curvature measurements obtained for a control wafer. The table shows in the first row, the initial

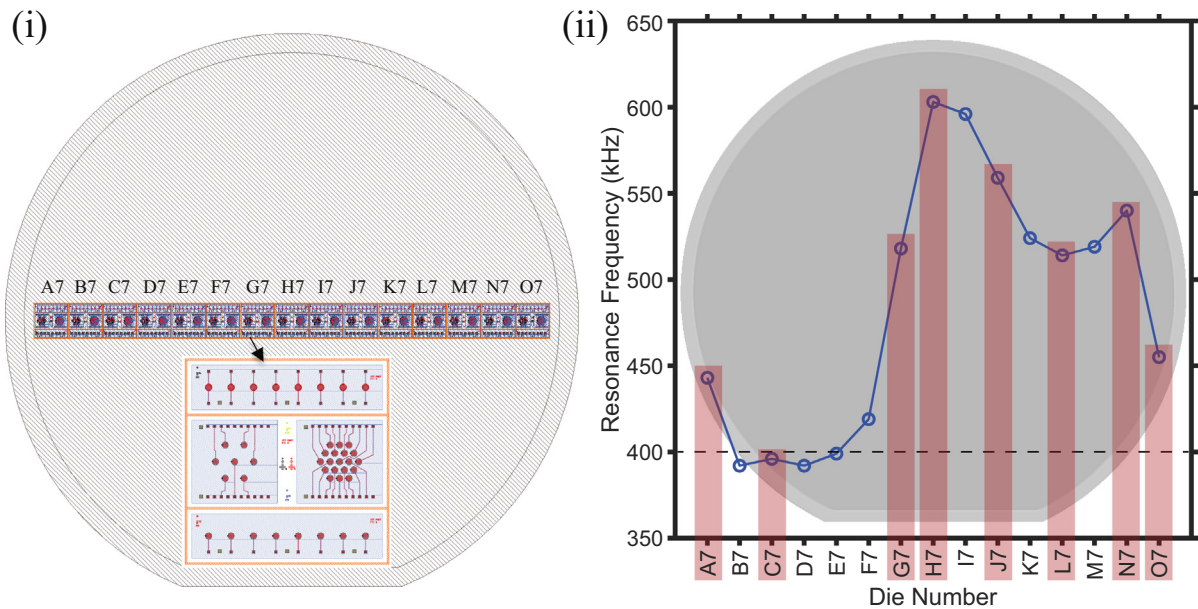


Fig. 4. (i) is a schematic of the wafer layout, coding of the diced chips and the structure of the 7-, 8-, and 19-element PMUT and (ii) is the results of the resonance frequency measurement across the wafer. The die numbers measured in this work are highlighted in red.

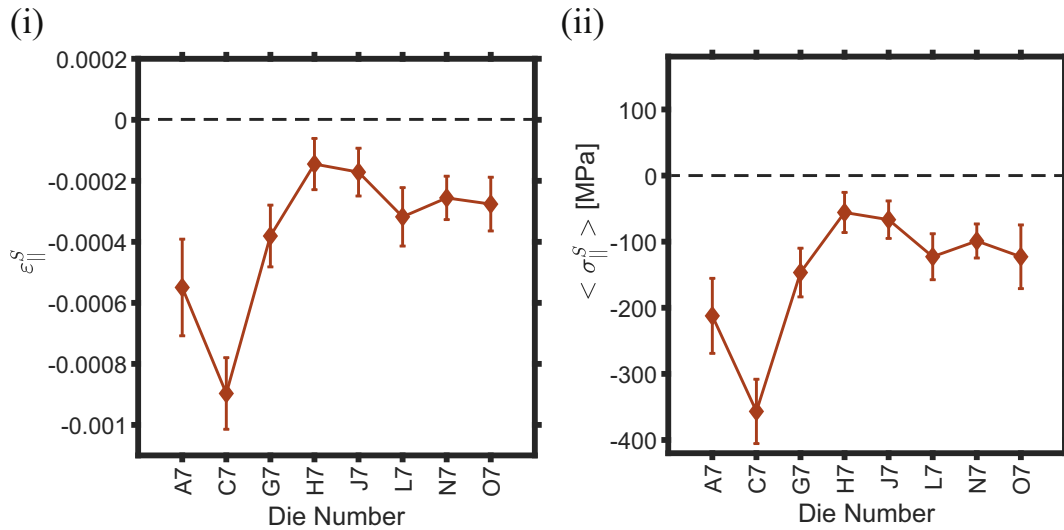


Fig. 5. Results of the biaxial in-plane (i) strain and (b) stress values for the samples as a function of position along the length of the wafer.

AlN passivation layer that is in biaxial in-plane tensile residual stress. The subsequent layers are designed in order to achieve a near zero biaxial in-plane residual stress; to achieve the Multiphysics modelled resonance frequency of 400 kHz. Final structural measurements showed a slight biaxial compressive residual stress in the thin-film stack, seen in the final row of Table 2.

Two XRD beam conditions were considered for reliably determining sample comparable lattice spacings, (i) the convergent focused beam condition, and (ii) the parallel beam condition. Both have several advantages and disadvantages that were considered. The focused beam method could allow for a small probe diameter with sufficient intensity allowing diffraction to occur mostly from the membrane. However, focused beam conditions can suffer from aberrations and peak shift challenges due to sample height alignment [18,25]. The parallel beam condition reduces or avoids any such issues, due to sample height alignment and aberrations, but can suffer from low intensity [26]. In this configuration the diffraction data was collected from the entire sample, and not just the membrane. Since the residual stress in the piezoelectric AlN layer was introduced during sputtering, the relevant residual stress would be also present in the surrounding membrane film. The parallel condition was chosen over the focused beam condition as it is more important to compare the stress-strain behavior between samples and eliminate any peak shifts due to sample misalignment.

The results of the in-plane strain and the biaxial in-plane residual stress for the samples as a function of position on the processed wafer can be seen in Fig. 5(i) and (ii), respectively. As seen in the figure, there is a clear trend from more to less compressive residual stress from the left-to-right hand side of the wafer. The same behavior is observed in the resonance frequency where a lower to higher resonance frequency is observed, as seen in Fig. 4(ii). The stress values observed in these samples are relatively low compared to literature values of investigated reactive magnetron AlN sputtering, which can vary in extreme cases to as large as -3 to $+1$ GPa [27–29].

The error bars in these figures are related to the fitting parameter errors from the least-squares fit. As more out-of-plane AlN poles, such as hk_2 , hk_3 , and $00l$, were unmeasurable (due to the lack of intensity) in the in-plane configuration, it could be expected that this could have the following affects: an effect on the magnitude of the residual stress and an increase in the error margin of each result. However, the impact of biaxial in-plane residual stress on the measured diffraction strain is more significant in the in-plane configuration. The strain-free lattice constants for w-AlN have been exhaustively studied, therefore there is a high degree of certainty in

values reported in the literature. Nevertheless, there is still variation in reported values. A consequence of this is a level of uncertainty in the reported absolute stress values. Similarly, discrepancies in the reported values of the single crystal stiffness tensor can introduce uncertainties and affect the absolute stress values.

Fig. 6 is a plot of the measured biaxial in-plane residual stress as a function of the measured resonance frequency. The fitted curve is the resonance frequency, as a function of residual stress from the classical plate theory for a circular plate. As the figure shows the trend between the model and the measured data, that follows the trend of higher compressive stresses results in a lower resonance frequency. Undoubtedly there are other contributions to the resonance frequency, such as the cavity diameter, as demonstrated by the data scatter. Nonetheless, the trend is clear. This work highlights the sensitivity of the resonance frequency and piezoelectric thin-film residual stresses. If the target resonance frequency is 400 kHz with a bandwidth of ± 3.1 kHz, this would result in a residual stress margin of ± 1.1 MPa. This is particularly applicable to PMUT devices where frequency matching requirements are critical to keep within the bandwidth [12].

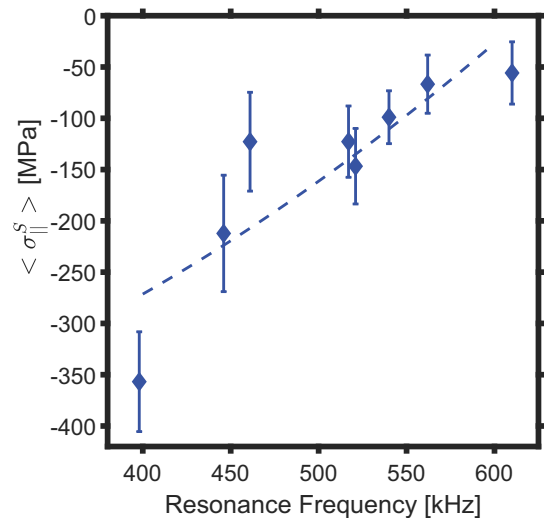


Fig. 6. Plot of the XRD measured biaxial in-plane residual stress as a function of the measured resonance frequency.

4. Conclusion

In summary, piezoelectric materials, such as AlN, exhibit several favorable qualities for resonating MEMS sensors and actuators. These include, reproducible film properties, CMOS process compatibility, and high hardness and stiffness properties. Reactive sputtering of AlN thin films for piezoelectric applications is the method of choice not only for film stress control but also process integration and ease of depositing the contact metallization within the same process. There are challenges nonetheless, relating to process control and residual stress uniformity, as this work has demonstrated.

PMUT devices exhibited a range of resonance frequencies, from under 400 kHz to a maximum of over 600 kHz. The initial hypothesis as to why these devices exhibited a wide range of resonance frequencies was the nonuniform residual stress parallel to the primary wafer flat. Therefore, this work examined the biaxial residual stress state of the PMUT devices as a function of position along the wafer, using XRD. Results revealed a range of compressive residual stress values ranging from -357 MPa to -56 MPa, which generally followed the behavior of the resonance frequency. In addition, the residual stress trend follows the classical plate theory for a circular plate where the pretension term (formed by residual stresses) is the dominant factor.

Finally, this work highlights the importance of not only process control, but also an understanding of the residual stress profile at the wafer-level. Often residual stresses are determined by wafer curvature measurements that provides an insight into the global stresses present. However, it is now abundantly clear that significant film nonuniformities can be present at the die-level. Methods that examine the crystalline state of a sample, such as XRD, are required in probing die-level stresses. In particular, in cases of resonating MEMS devices built on piezoelectric thin films where strict film properties are required.

Data availability

The raw/processed data required to reproduce these findings are available to download from the corresponding author.

Credit author statement

Glenn Ross: Conceptualization, Methodology, Validation, Formal analysis, Investigation, Resources, Data Curation, Writing - Original Draft, Writing - Review & Editing, Visualization.

Hongqun Dong: Investigation, Resources, Writing - Review & Editing.

Cyril Baby Karthedath: Resources, Writing - Review & Editing, Visualization.

Abhilash Thanniyil Sebastian: Resources, Writing - Review & Editing, Visualization.

Tuomas Pensala: Project administration, Funding acquisition.

Mervi Paulasto-Kröckel: Supervision, Writing - Review & Editing, Project administration, Funding acquisition.

Declaration of Competing Interest

The authors declare that they have no known competing financial interests or personal relationships that could have appeared to influence the work reported in this paper.

Acknowledgments

This work is part of the POSITION-II project funded by the ECSEL Joint Undertaking under grant number Ecse1-783132- Position-II-

2017-IA. The authors would like to acknowledge the Innovation Funding Agency Business Finland for their financial support. We acknowledge the provision of facilities and technical support by Aalto University at OtaNano-Nanometroscopy Center (Aalto-NMC).

References

- [1] M. Tilli, M. Paulasto-Kröckel, M. Petzold, H. Theuss, T. Motooka, V. Lindroos, *Handbook of Silicon Based MEMS Materials and Technologies*, Third edition, 2020.
- [2] H. Bhugra, G. Piazza, *Piezoelectric MEMS resonators*, Springer, 2017.
- [3] M.T. Todaro, F. Guido, V. Mastronardi, D. Desmaele, G. Epifani, L. Algieri, M. De Vittorio, Piezoelectric MEMS vibrational energy harvesters: advances and outlook, *Microelectron. Eng.* 183–184 (2017) 23–36, <https://doi.org/10.1016/j.mee.2017.10.005>.
- [4] A. Hajati, D. Latev, D. Gardner, A. Hajati, D. Imai, M. Torrey, M. Schoeppler, Three-dimensional micro electromechanical system piezoelectric ultrasound transducer, *Appl. Phys. Lett.* 101 (2012) 253101, <https://doi.org/10.1063/1.4772469>.
- [5] P. Zhang, G. Fitzpatrick, T. Harrison, W.A. Moussa, R.J. Zemp, Double-soi wafer-bonded CMUTs with improved electrical safety and minimal roughness of dielectric and electrode surfaces, *J. Microelectromech. Syst.* 21 (2012) 668–680, <https://doi.org/10.1109/JMEMS.2012.2189358>.
- [6] Y. Lu, H.Y. Tang, S. Fung, B.E. Boser, D.A. Horsley, Pulse-Echo ultrasound imaging using an AlN piezoelectric micromachined ultrasonic transducer Array with transmit beam-forming, *J. Microelectromech. Syst.* 25 (2016) 179–187, <https://doi.org/10.1109/JMEMS.2015.2503336>.
- [7] A. Iqbal, F. Mohd-Yasin, Reactive sputtering of aluminum nitride (002) thin films for piezoelectric applications: A review, *Sensors (Switzerland)* 18 (2018) 1797, <https://doi.org/10.3390/s18061797>.
- [8] M.A. Dubois, P. Murali, Stress and piezoelectric properties of aluminum nitride thin films deposited onto metal electrodes by pulsed direct current reactive sputtering, *J. Appl. Phys.* 89 (2001) 6389–6395, <https://doi.org/10.1063/1.1359162>.
- [9] A. Dangi, R. Pratap, System level modeling and design maps of PMUTs with residual stresses, *Sensors Actuators A Phys.* 262 (2017) 18–28, <https://doi.org/10.1016/j.sna.2017.05.006>.
- [10] F. Sammoura, K. Smyth, S. Bathurst, S.G. Kim, An analytical analysis of the sensitivity of circular piezoelectric micromachined ultrasonic transducers to residual stress, *IEEE Int. Ultrason. Symp. IUS* (2012) 580–583, <https://doi.org/10.1109/ULTSYM.2012.0144>.
- [11] P. Murali, N. Lederemann, J. Paborowski, A. Barzegar, S. Gentil, B. Belgacem, S. Petitgrand, A. Bosseboef, N. Setter, Piezoelectric micromachined ultrasonic transducers based on PZT thin films, *IEEE Trans. Ultrason. Ferroelectr. Freq. Control* 52 (2005) 2276–2288, <https://doi.org/10.1109/TUFFC.2005.1563270>.
- [12] C.B. Karthedath, A.T. Sebastian, J. Saarihi, T. Sillanpaa, T. Pensala, Design and Fabrication of Aluminum Nitride Piezoelectric Micromachined Ultrasonic Transducers for Air Flow Measurements, in: *IEEE Int. Ultrason. Symp. IUS*, 2019, <https://doi.org/10.1109/ULTSYM.2019.8925544>.
- [13] H.W. King, E.A. Payzant, Error corrections for x-ray powder diffractometry, *Can. Metall. Q.* 40 (2001) 385–394, <https://doi.org/10.1179/cmq.2001.40.3.385>.
- [14] M.A. Moram, M.E. Vickers, X-ray diffraction of III-nitrides, *Rep. Prog. Phys.* 72 (2009), 036502, <https://doi.org/10.1088/0034-4885/72/3/036502>.
- [15] B.D. Cullity, *Elements of X-Ray Diffraction*, 2nd edition, 1978.
- [16] B.H. Toby, R.B. Von Dreele, GSAS-II: the genesis of a modern open-source all purpose crystallography software package, *J. Appl. Crystallogr.* (2013), <https://doi.org/10.1107/S0021889813003531>.
- [17] H. Schulz, K.H. Thiemann, Crystal Structure Refinement of AlN and GaN, *Solid State Commun.* 1977, [https://doi.org/10.1016/0038-1098\(77\)90959-0](https://doi.org/10.1016/0038-1098(77)90959-0).
- [18] I.C. Noyan, J.B. Cohen, Residual Stress - Measurement by Diffraction and Interpretation, 1987, <https://doi.org/10.1002/crat.2170240228>.
- [19] W. Paszkowicz, S. Podsiadło, R. Minikayev, Rietveld-refinement study of aluminium and gallium nitrides, *J. Alloys Compd.* 382 (2004) 100–106, <https://doi.org/10.1016/j.jallcom.2004.05.036>.
- [20] U. Welzel, J. Ligot, P. Lamparter, A.C. Vermeulen, E.J. Mittemeijer, Stress analysis of polycrystalline thin films and surface regions by X-ray diffraction, *J. Appl. Crystallogr.* 38 (2005) 1–29, <https://doi.org/10.1107/S0021889804029516>.
- [21] J.M. Zhang, Y. Zhang, K.W. Xu, V. Ji, Anisotropic elasticity in hexagonal crystals, *Thin Solid Films* 515 (2007) 7020–7024, <https://doi.org/10.1016/j.tsf.2007.01.045>.
- [22] H. Dölle, The influence of multiaxial stress states, stress gradients and elastic anisotropy on the evaluation of (residual) stresses by X-rays, *J. Appl. Crystallogr.* 12 (1979) 489–501, <https://doi.org/10.1107/s0021889879013169>.
- [23] C.E. Murray, Equivalence of Kröner and weighted Voigt-Reuss models for x-ray stress determination, *J. Appl. Phys.* 113 (2013), <https://doi.org/10.1063/1.4801917>.
- [24] K. Tsubouchi, N. Mikoshiba, Zero-temperature-coefficient SAW devices on AlN epitaxial films, *IEEE Trans. Sonics Ultrason.* SU-32 (1985) 634–644, <https://doi.org/10.1109/T-SU.1985.31647>.
- [25] V. Hauk, *Structural and Residual Stress Analysis by Nondestructive Methods*, Inst. Mater. London, UK, 1997, <https://doi.org/10.1016/B978-0-44482476-9/50000-1>.
- [26] M. Leoni, U. Welzel, P. Scardi, Polycapillary optics for materials science studies: instrumental effects and their correction, *J. Res. Natl. Inst. Stand. Technol.* 109 (2004) 27–48, <https://doi.org/10.6028/jres.109.003>.
- [27] E. Iborra, M. Clement, J. Sangrador, A. Sanz-Hervás, L. Vergara, M. Aguilar, Effect of particle bombardment on the orientation and the residual stress of sputtered AlN

- films for SAW devices, IEEE Trans. Ultrason. Ferroelectr. Freq. Control 51 (2004) 352–358, <https://doi.org/10.1109/TUFFC.2004.1320791>.
- [28] S.H. Lee, K.H. Yoon, D.S. Cheong, J.K. Lee, Relationship between residual stress and structural properties of AlN films deposited by r.f. reactive sputtering, Thin Solid Films 435 (2003) 193–198, [https://doi.org/10.1016/S0040-6090\(03\)00353-5](https://doi.org/10.1016/S0040-6090(03)00353-5).
- [29] H.Y. Liu, G.S. Tang, F. Zeng, F. Pan, Influence of sputtering parameters on structures and residual stress of AlN films deposited by DC reactive magnetron sputtering at room temperature, J. Cryst. Growth 363 (2013) 80–85, <https://doi.org/10.1016/j.jcrysgro.2012.10.008>.